

Full Length Article

The effect of multi-beam strategies on selective laser melting of stainless steel 316L



Thorsten Heeling*, Konrad Wegener

Institute of Machine Tools and Manufacturing, ETH Zurich, 8092 Zurich, Switzerland

ARTICLE INFO

Keywords:
 Selective laser melting
 Powder bed fusion
 Direct metal laser sintering
 Additive manufacturing
 Multi-beam strategies
 Stainless steel

ABSTRACT

With increasing industrial application of additive manufacturing technologies, such as selective laser melting, the requirements concerning the processes' capabilities like productivity, robustness, part quality and the range of processable materials are increasing as well. But due to high cooling rates, high thermal gradients and a layer-wise processing, parts produced by selective laser melting are subject to different kinds of defects. These defects commonly lead to high porosity, distortion, cracking and rough surfaces. But when a second beam is used to heat the vicinity of the melt pool a homogenization of the temperature field, a reduction of the cooling speeds within the melt pool and in its vicinity as well as an improved wetting behavior is possible. A proof of concept is shown, discussing general trends and possibilities, like increased surface qualities or dense microstructures with low amounts of remelting, when these strategies are elaborated.

1. Introduction

Selective laser melting (SLM) is a fairly young technology for the additive manufacturing (AM) of complex parts made of metal alloys. The parts are built using a layer-wise process starting with an incremental movement of the build plate by one layer thickness. On that build plate a thin layer of metal powder particles is distributed and afterwards selectively irradiated by a laser beam so that the necessary cross sections are molten, resulting in a nearly fully-dense part. Due to the use of a highly focused laser beam high temperature gradients and cooling speeds as well as evaporation and spattering arise in and around the melt pool. While high temperature gradients and cooling speeds lead to high residual stresses, distortion and cracking [1–3], evaporation and spattering increase the probability of microstructural defects like gaseous pores or a lack of fusion and decrease the surface quality [4–6]. These issues significantly reduce the usability of additively manufactured parts. Nevertheless a range of different materials like steels, nickel-, aluminum-, titanium- and cobalt-based alloys already have been qualified for the SLM process [7–12]. Furthermore, extensive work has been put in the quantification of the material's static and dynamic tensile behavior [13–16] and the understanding of the underlying physical effects [17–20].

1.1. Multi-beam strategies

Only little research is available for multi-beam strategies in SLM.

For direct metal deposition Aggarangsi and Beuth [21] simulative showed that a preheating beam can reduce the maximum stresses by 20% to 30%. Wilkes et al. [22] used a stationary second beam to increase the overall temperature of the powder bed to temperatures as high as 1800 °C to reduce temperature gradients and thus making ceramics processable. Furthermore, experiences from the additive manufacturing process of electron beam melting show that residual stresses and distortion can be lowered by heating the surrounding of the melt pool and therefore lowering the temperature gradients. Abe et al. [23] showed in early experiments that the maximum bending strength and hardness can be increased when a melting beam is followed by a second widened beam. But no follow-up seems to be available despite the promising results. In Heeling et al. [24,25] simulative and preliminary experimental results showed that multi-beam strategies in SLM are feasible and are able to reduce stresses without loosing a significant amount of productivity per laser power. To deepen the knowledge about multi-beam strategies in SLM and to establish a common basis for further work an investigation into the influence of melt pool shapes, the smoothness of tracks and the resulting density is presented in this paper.

2. Experimental set-up

2.1. Laboratory machine

The experiments are conducted on a self-developed SLM laboratory

* Corresponding author.

E-mail address: heeling@iwf.mavt.ethz.ch (T. Heeling).

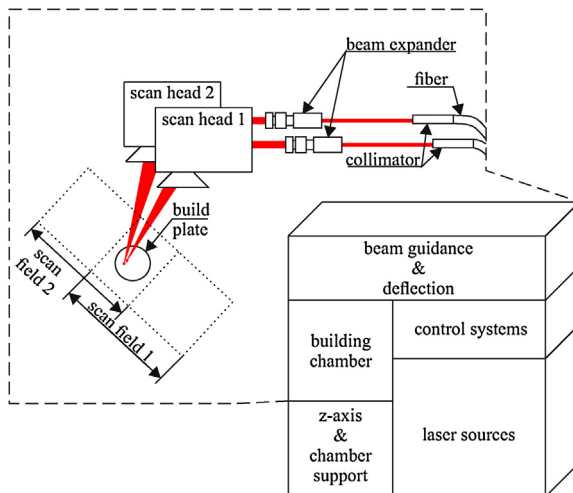


Fig. 1. Illustration of the laboratory machine's configuration to achieve a wide overlap of the scan fields.

machine featuring all essential functions as well as two water-cooled 200 W fiber lasers of 1070 nm wavelength (IPG YLR-200-WC) and two independently controllable scan heads (SCANLAB hurrySCAN III 14) with f-theta optics of 420 mm effective focal length. By positioning the scan heads right next to each other, a scan field overlap of 160 mm × 280 mm can be achieved. For the multi-beam experiments a build plate with a diameter of 100 mm is put in the center of the overlap as depicted in Fig. 1.

A self-developed path planning tool is used to generate the G-code which is interpreted by the control system (Aerotech A3200) to deflect the beams and irradiate the cross sections. This allows an independent control of both scan heads as well as synchronized movement.

2.2. Elaborated multi-beam strategies

The presented multi-beam strategies are intended to influence the temperature field in and around the melt pool so that the solidification process can be influenced at an optimal usage of the input power. Offset strategies revealed themselves to be the most promising ones to achieve this goal without the necessity of extensive tool path planning [24]. The offset strategies are defined by a fixed offset of the first (melting beam) to the second laser beam (heating beam). If the heating beam moves in front of the melting beam, preheating of the melt pool's vicinity as well as a premelting of a small amount of powder particles can be established. In case the heating beam moves behind the melting beam, postheating can be used to homogenize the temperature field in the back of the melt pool as well as reducing the cooling speeds due to a second heat input after the melting laser passed by. Both, preheating and postheating are illustrated in Fig. 2.

2.3. Calibration process

The coordinate systems of both scan heads have to match within the build plane so that a reliable positioning of both laser beams to each other can be guaranteed. Therefore a calibration process is performed prior to the build process in which the coordinate system of the heating beam's scan head is adjusted to match the one of the melting beam's scan head. This is done by marking crosses at different positions of the build plate with both systems so that a location dependent displacement of the coordinate system can be measured. This data is used to correct the scan heads calibration file, so that the displacement all over the build plate is reduced to a practical residual error smaller than 20 µm in x and y.

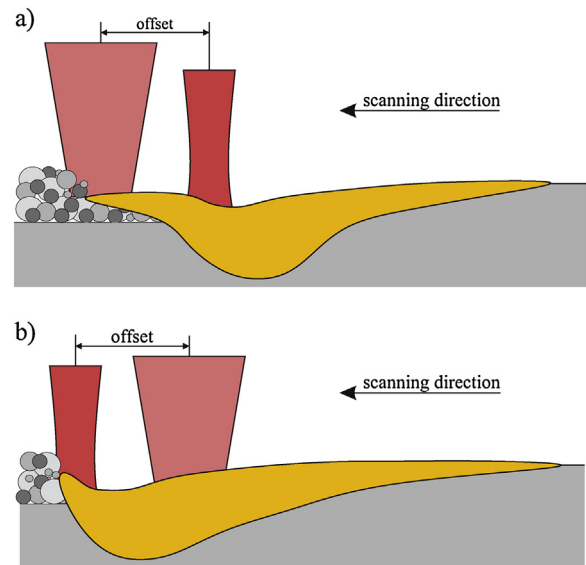


Fig. 2. Longitudinal sections depicting (a) preheating and (b) postheating. The heating beam is defined by a significantly wider spot size than the melting beam.

2.4. Experimental design

Preheating and postheating were investigated using a melting beam constantly focused to 90 µm and a defocused heating beam, whose focal plane is moved below the working plane, at two different diameters, either 270 µm or 380 µm. This guarantees similar maximum intensities for sets of 270 µm at 100 W and 380 µm at 200 W.

All variable parameters which were used to build cubic samples of stainless steel 316L are listed in Table 1. The melting beam is always operated using its maximum power of 200 W at 90 µm spot size and 82.5 µm hatch distance while the layer thickness is set to 30 µm. Single-beam reference cubes were built without using the heating beam. All samples were built using an alternating scanning pattern, so that the scanning direction was rotated by 90° after every single layer. Furthermore all samples use the same dense parameter set of 200 W laser power and 1000 mm/s scan speed at 90 µm for the contour to allow reliable density measurements. The densities are evaluated using the Archimedes principle, measuring the sample's mass in air and in acetone. The cross sections are ground, polished and etched for 120 s in V2A etchant before being imaged on an Alicona InfiniteFocus using a 20× magnification. The V2A etchant contains about 47.5 vol% distilled water, 47.5 vol% hydrochloric acid (32%), 4.9 vol% nitric acid (65%) and 0.1 vol% Vogel's special reagent.

The top surfaces are evaluated using a Leica DCM3D with 20× magnification, imaging an area of 2.36 mm × 1.77 mm. Within this

Table 1

Overview of parameter sets used for the hatching of cubic samples of stainless steel 316L. d_h is the heating beam spot diameter, P_h the heating beam's laser power, v the scan speed and Δx the beam offset.

	d_h [µm]	P_h [W]	v [mm/s]	Δx [µm]
Reference				1000, 1250, 1500, 1750, 2000
Preheating	270	100	1000, 1250, 1500	-45, -90, -180, -270
	380	200	1000, 1500, 1750, 2000	-45, -90, -180, -270
Postheating	270	100	1000, 1250, 1500	45, 90, 180, 270, 360, 450
	380	200	1000, 1500, 1750, 2000	45, 90, 180, 270, 360, 450

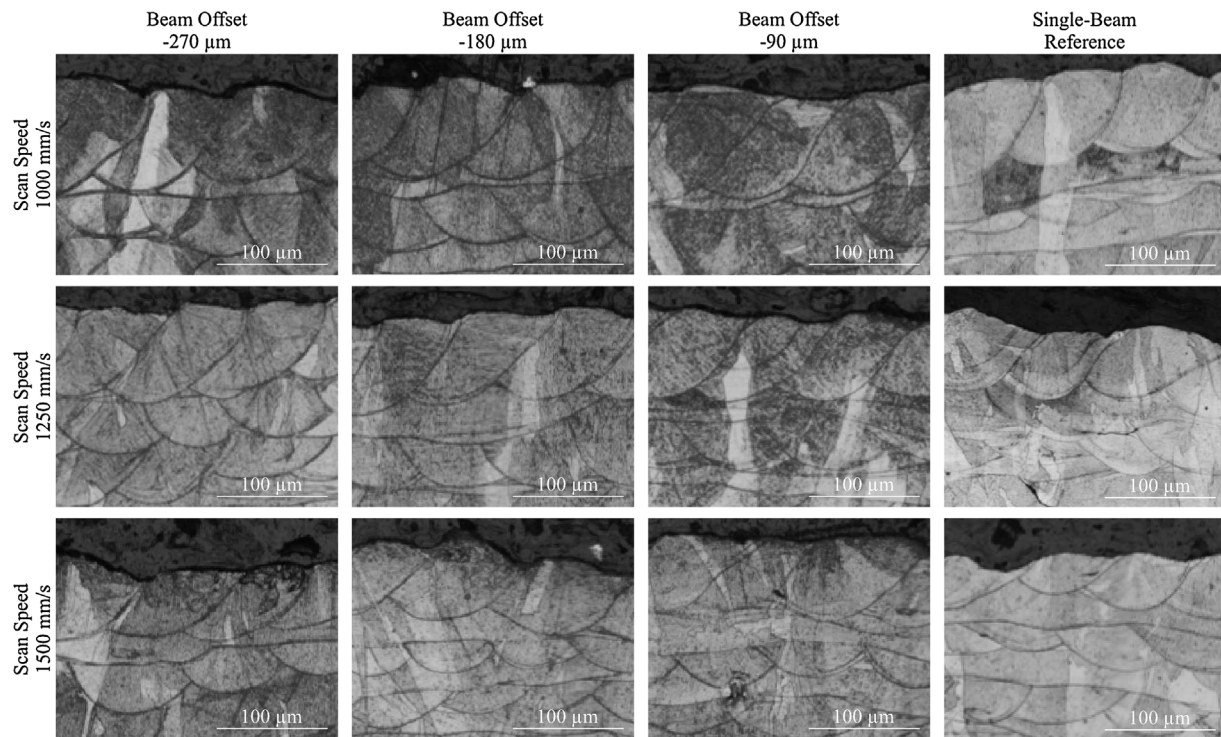


Fig. 3. Melt pool cross sections of single-beam reference samples as well as preheating multi-beam samples with a heating beam of 270 μm beam diameter and 100 W heating power. Beam offsets of 45 μm are not shown.

area ten roughness profiles are assessed perpendicular to scanning direction and equally distributed over the imaged area. Those profiles are used to calculate the arithmetical mean deviation of the surface roughness. The key interest lays within the smoothness of the overlap of neighboring melt pools. Therefore waviness due to effects like spatter or imperfections of the recoating device is filtered by using a cut-off length of 0.25 mm. This value is chosen as about three times the hatch distance to make sure that the surface roughness due to the curvature of solidified tracks is not removed but only the waviness due to spatter and flawed powder beds. This cut-off length is elaborated automatically by the Leica DCM3D software as defined in the ISO4288 standard.

3. Results and discussion

3.1. Resulting melt pool shapes

The melt pool cross sections that are measured in the cubic samples offer a chance to investigate the melt pool dimensions and the effects that might have led to the results quantified in the measured surface roughness and density. As references the single-beam samples of the corresponding scan speeds were used. In Figs. 3 and 4 melt pool cross sections of the preheating parameter sets as well as single-beam references are illustrated. The reference samples show that the melt pool dimensions of 1000 mm/s and 1250 mm/s are comparable. But starting at 1500 mm/s the melt pool dimensions, especially the melt pool depth, continuously decrease. The melt pool dimensions and the amount of remelting are smaller due to the lower amount of energy density that is provided to melt the powder material as well as previous layers and tracks. The low amount of remelting at higher scan speeds leads to an insufficient wetting of the previous layer, large contact angles and therefore a stronger influence of the capillary forces which results in spherical, droplet-like melt pools. The bad wetting between neighboring tracks and the low rate of remelting increase the chance of defects, especially that of lack of fusion.

The trend of decreasing melt pool depth for increasing scan speeds can as well be seen for all multi-beam samples. In case of the preheating

strategy, Figs. 3 and 4, the general melt pool shapes are comparable to those of a single-beam with the same overall energy density. The melt pools are mostly half-spherical, with larger dimensions than the same speed reference samples. For same speed samples the larger melt pool dimensions can be explained by the additional amount of energy that is provided by the heating beam. But due to the significantly wider beam diameter of the heating beam the width to depth ratio of the multi-beam strategies is larger. In case of a heating beam diameter of 380 μm and 1000 mm/s scan speed, Fig. 4, the melt pools show a significant widening of the upper melt pool part up to roughly twice the size of the reference melt pools. Therefore it can be assumed that for these parameter sets the intensity of the heating beam is large enough to melt material far wider than the melting beam reaches, resulting in a large melt pool overlap in the upper third of the melt pool. In case of a 270 μm heating beam, Fig. 3, no similar effect can be observed.

Compared to the postheating parameter sets of the same speed, that are depicted in Figs. 5 and 6, the postheating melt pools show slightly larger dimensions, although they are comparable for low offsets. Here again the influencing factor is the amount of energy that is available to melt the material. While for preheating parameter sets the heating energy already induced a temperature increase when the melting beam irradiates the material, for postheating the energy is provided not earlier than in the moment when the maximum melt pool dimensions are reached. In case of low offsets of the postheating strategy the heating beam overlaps with the melting beam and is therefore increasing the available melting power so that the dimensions are enlarged. But in case of larger offsets there is no significant overlap of the two beams and the energy is in fact provided when the melt pool is already cooling down. That is why double melt pool boundaries can be observed for large offsets of the postheating strategies. In these cases the energy provided by the heating beam is stopping the solidification or is even remelting a small part of the recently solidified material. This is supported by the fact that the upper melt pool boundary is far wider than the lower one while the shape and depth of the lower melt pool boundary is comparable to the one of the reference single-beam cross sections. The double melt pools start at roughly 180 μm offset for both

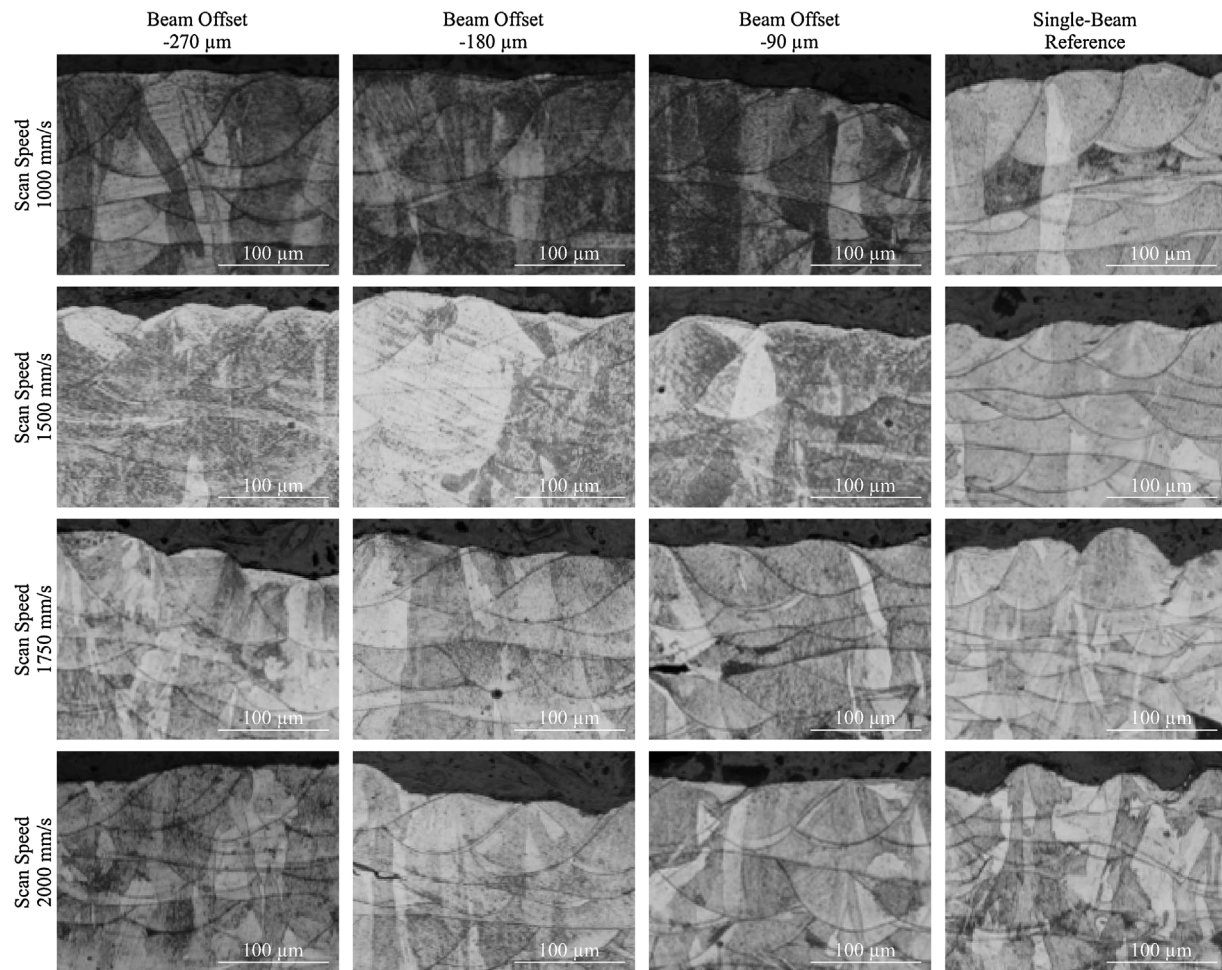


Fig. 4. Melt pool cross sections of single-beam reference samples as well as preheating multi-beam samples with a heating beam of 380 μm beam diameter and 200 W heating power. Beam offsets of 45 μm are not shown.

heating beam diameters. The starting point of this effect is independent of the scan speed. The distance between the lower and the upper melt pool boundary is increasing with increasing offsets but decreases for increasing scan speeds. This supports the assumption that the heating beam is responsible for the second melt pool boundary. Because at higher offsets the material is cooling down for a longer time before the heating beam irradiates the material again. Therefore the depth that is not influenced by the heating beam is larger which leads to a larger distance between lower and upper melt pool boundary. In case of higher scan speeds the first melt pool is less deep due to the lower provided energy density. Also the time between the irradiation by the melting beam and the heating beam is shorter due to the higher scan speeds, which as well is the reason why the distance between the lower and upper melt pool boundary is decreased.

In case of the postheating strategy also a smoothing of the surface by the second beam can be observed, especially for high beam offsets and high heating beam powers as can be seen in Fig. 6. This enables very high scan speeds of up to 2000 mm/s to be used without any balling, although the melt pool depths are very small. This is because the irradiation by the heating beam can be considered a remelting of the surface which is known to reduce the surface roughness and the probability for defects. The smooth surfaces significantly decrease the chance of defects in the microstructure. So using this strategy samples can be manufactured with a very small amount of remelted volume.

3.2. Resulting surfaces

Because of the top surface's dependency of spatter, the recoater's and the previous layer's imperfections and therefore a dependency of the part positioning, irradiation sequence and random effects, the imaged surfaces are filtered with a cut-off length of 0.25 mm. This results in an image in which just the melt pool curvature of neighboring tracks is available. Therefore the surface roughness values of the filtered images are an indicator for the wetting of the melt to neighboring tracks and the minimum resulting surface roughness that can be achieved under ideal process conditions. The difference between unfiltered and filtered images is illustrated in Fig. 7.

The results of the arithmetical mean deviation of surface roughness R_a are plotted in Fig. 8 for all investigated parameter sets. The results show that a heating beam of 100 W power and 270 μm diameter on the surface roughness follows no general trend. The changes to the surface roughness when using multi-beam strategies with this heating beam configuration are mostly within the measured standard deviation. This matches the observation made using the micrographs that when using this heating beam configuration the influence on neighboring tracks is neglectable. In contrast, a significant influence can be seen when using the parameter set of a higher heating power of 200 W at a diameter of 380 μm . In these cases R_a is reduced by about 50% for slow scan speeds with already good surface qualities and by about 70% for fast scan speeds that would result in surfaces with balling when being used with a single beam of 200 W and 90 μm diameter. A far lower surface roughness is achieved for most offsets. In case of the very small offsets it

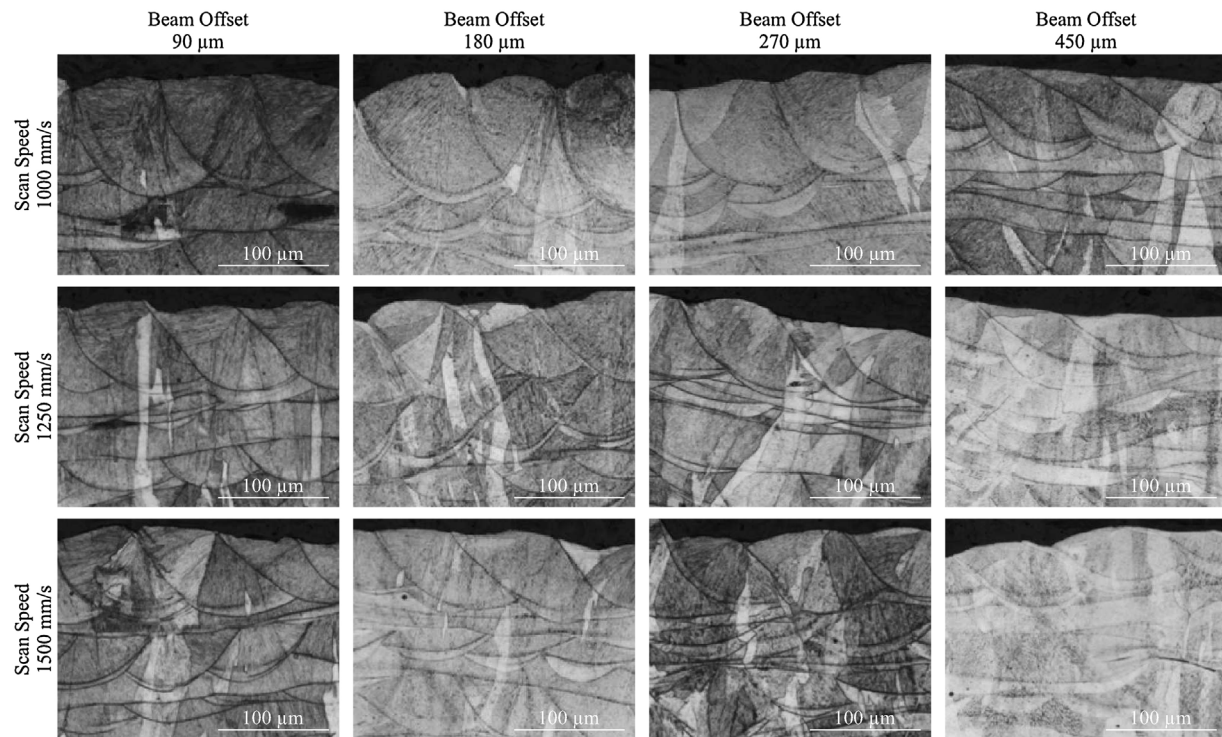


Fig. 5. Melt pool cross sections of postheating multi-beam samples with a heating beam of 270 μm beam diameter and 100 W heating power. Beam offsets of 45 μm and 360 μm are not shown.

can be assumed that the additional heating power is leading to a melting of larger regions of previous tracks and therefore increasing the wetting of the melt at its largest dimensions which then results in a lower surface roughness. In case of very large postheating offsets the connection of the new layer to the previous ones is established by the melting beam, while the heating beam results in a slower cool down of the upper melt pool parts and a remelting of surrounding solidified material. It can be assumed that especially the remelting of already solidified melt results in a smoother surface. This is supported by the micrographs that show very wide remelted areas for small offsets and double melt pools for large offsets. The difference between medium sized offsets of preheating and postheating might be explained with a look into the spatter characteristics, as described in Heeling et al. [26]. Because when preheating is used, the spatter count is far lower than for postheating strategies. Less spatter is an indicator for a more stable process because of a smaller chance that spatter is accelerated back on the part or that spatter is crossing the incident laser energy and therefore disturbing the melting process. The smaller standard deviations of the arithmetical mean deviation for preheating strategies are supporting the assumption that in these cases the process is more stable.

3.3. Effect on density

The measured relative densities of the single- and multi-beam samples are illustrated in Fig. 9. The measured densities are set in relation to the density of a nearly fully-dense sample produced by a single beam of 200 W and 1000 mm/s. Preheating strategies are listed as negative offsets and postheating strategies as positive offsets. The different colors indicate different levels of energy density.

The diagrams show that the density of the multi-beam samples can be higher than the reference density in case of higher energy densities. The maximum is at 100.58% of the reference cube's density which is reached for a heating beam of 200 W power and 380 μm diameter moving at 1000 mm/s with an offset of 90 μm . Taking a look into the micrographs it is obvious that this parameter set is one of those with the largest melt pool dimensions and largest melt pool overlaps. This is due

to the highest used energy density at a fairly low offset. The large melt pools and high remelting rates significantly reduce the probability for interlayer errors, offer a chance for gaseous pores to leave the melt pool and are therefore resulting in the highest densities. At the same speed as the reference cube the density values converge to the reference value for high offsets. This is reasonable since in these cases the melting beam is more or less independent of the heating beam and therefore the resulting density should be equally high. In these cases the heating beam slows down the solidification of the upper melt pool regions and smooths the surface. For faster scan speeds the density is lower than the reference density, even for those cases in which the energy density is higher. The lowest values are at 98.15% for a 270 μm heating beam and at 96.59% for a 380 μm heating beam, both at reference energy density but at speeds of 1500 mm/s and 2000 mm/s. The lowest values are always achieved when the largest offsets are used because the energy is distributed over a far larger area than it is the case for small offsets. In case of small offsets the density values are near to the reference cube's density for higher as well as equal energy densities. For example at 90 μm postheating offset, 270 μm heating beam diameter and 1500 mm/s and therefore an equally high energy density the resulting density is at 99.60% of the reference density. This is worth mentioning since the 100 W of heating power are distributed over a nine times larger area than the melting power. Furthermore, this explains why for higher heating beam diameters higher energy densities are necessary to reach the same level of density.

The diagrams show small plateaus of quasi-constant density values for different offsets. A significant effect of the scan speed as well as the beam diameter and heating power can be observed. For a 270 μm beam at 100 W and 1000 mm/s the plateau on the postheating side reaches from 45 μm to 360 μm . But at 1500 mm/s the width is reduced to a range from 90 μm to 270 μm and with a set of a beam diameter of 380 μm and a heating power of 200 W at 2000 mm/s it is further reduced to a range from 90 μm to 180 μm . The density values usually decrease for increasing beam offsets, as soon as the mentioned plateaus end. As the micrographs show, the plateaus are linked to melt pools of similar size and shape. Since for slower scan speeds the interaction

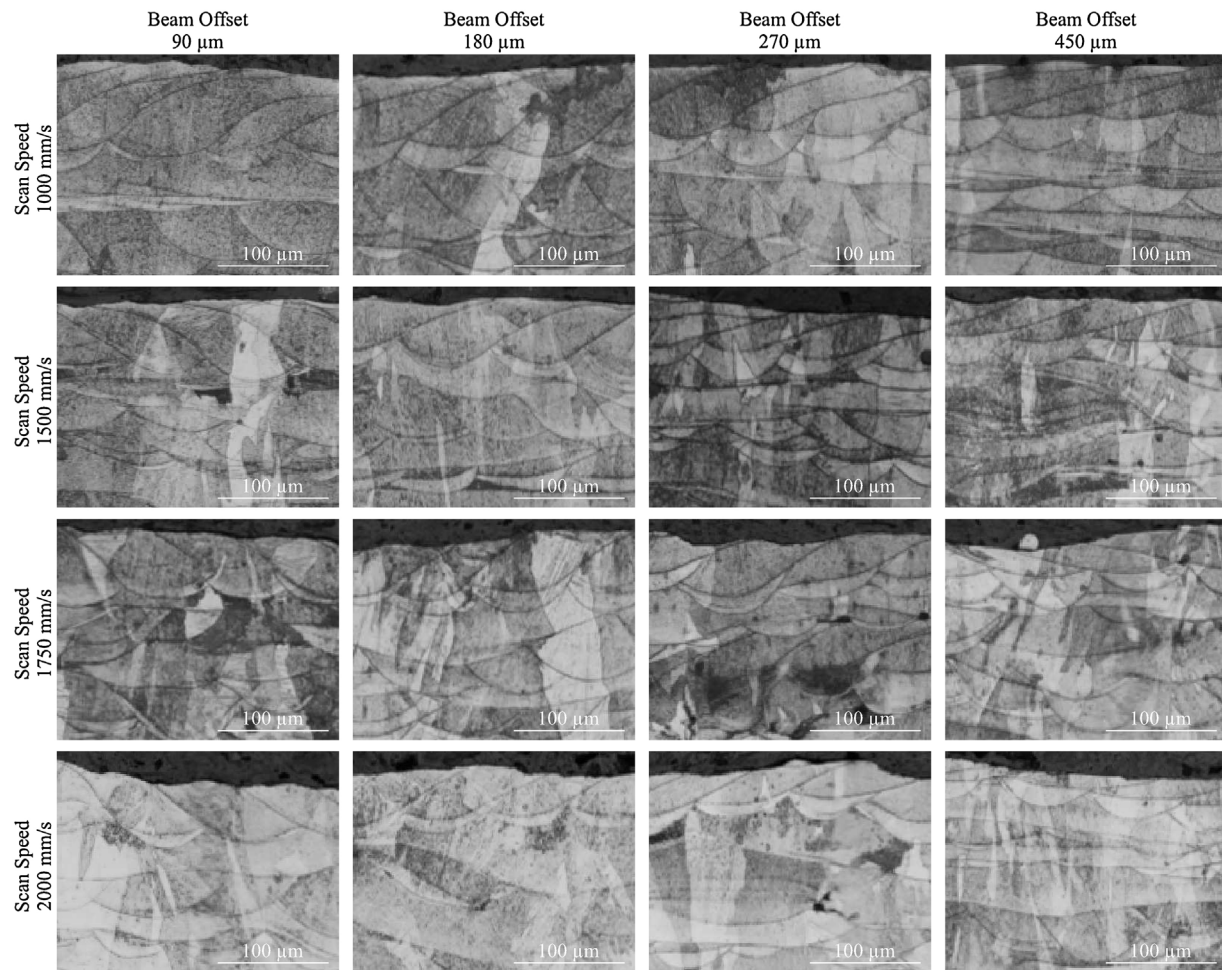


Fig. 6. Melt pool cross sections of postheating multi-beam samples with a heating beam of 380 μm beam diameter and 200 W heating power. Beam offsets of 45 μm and 360 μm are not shown.

times are longer, these parameter sets are less sensitive to a change in the offset. Therefore the plateaus are larger in these cases. In contrast to that the melt pool dimensions of higher scan speeds are already on the edge to what is necessary to result in a dense microstructure. So in these cases the density is more sensitive to a reduction of the power that is available to achieve maximum melt pool dimensions.

The maximum density values are always reached for beam offsets of 90 μm instead of 45 μm , for postheating as well as preheating. This effect could already be observed in preliminary experiments. It is assumed that for offsets smaller than 90 μm the beams are more extensively interfering with the evaporated material that is generated by the beam that is in front. This interaction would decrease the energy that reaches the melt pool and therefore reduce the melt pool dimensions. The micrographs support this assumption as the 45 μm offset parameter sets often show smaller melt pools than the 90 μm offset parameter sets.

A comparison of the pre- and postheating parameter sets with the same offset shows that the density values of the postheating strategies are slightly higher compared to those of the preheating strategies, although the micrographs show that the melt pool dimensions of the preheating parameter sets are usually larger than those of the post-heating sets. But considering that in case of postheating the heating beam reduces the cooling speeds it can be assumed that the melt pool lifetime is longer, increasing the chance for gaseous pores to leave the melt. Furthermore, heat conduction is given more time to establish a good bonding to the previous layer and track as well as the surface roughness is reduced so that the chance for interlayer defects is

decreased.

4. Effect on cool down phase

The presented strategies, especially the postheating strategy, undoubtedly influence the cool down of the melt pool depending on the actual offset. The most notable change which is a result of that and can be seen in the presented cross sections at large offsets are double melt pool boundaries. These are assumed to be the result of the melt pool's solidification which is stopped or even reversed by the second beam. To investigate this in more detail a simulation tool is elaborated to take a look in the temperature curves during cool down. The simulation tool is described in detail in [27].

Fig. 10 shows the simulated temperature development when using a 100 W, 270 μm wide heating beam at different postheating offsets. The influence of the heating beam on the temperature curves can be clearly seen by a second peak within the cool down phase. The distance of the main peak which is the result of the melting beam to the second peak is obviously depending on the chosen beam offset. While at 90 μm and 180 μm the second peak only results in changes in the still molten elements but not the already solidifying ones, the probability for double melt pool boundaries at these parameters is quite low. At 270 μm the second heat input results in a stopped solidification, defined by temperature curves which are parallel to the dashed line, which indicates melting temperature, while the heating beam is passing by. At 360 μm and 450 μm the second beams heat input results in the remelting of already solidified elements, indicated by lines which raise over the

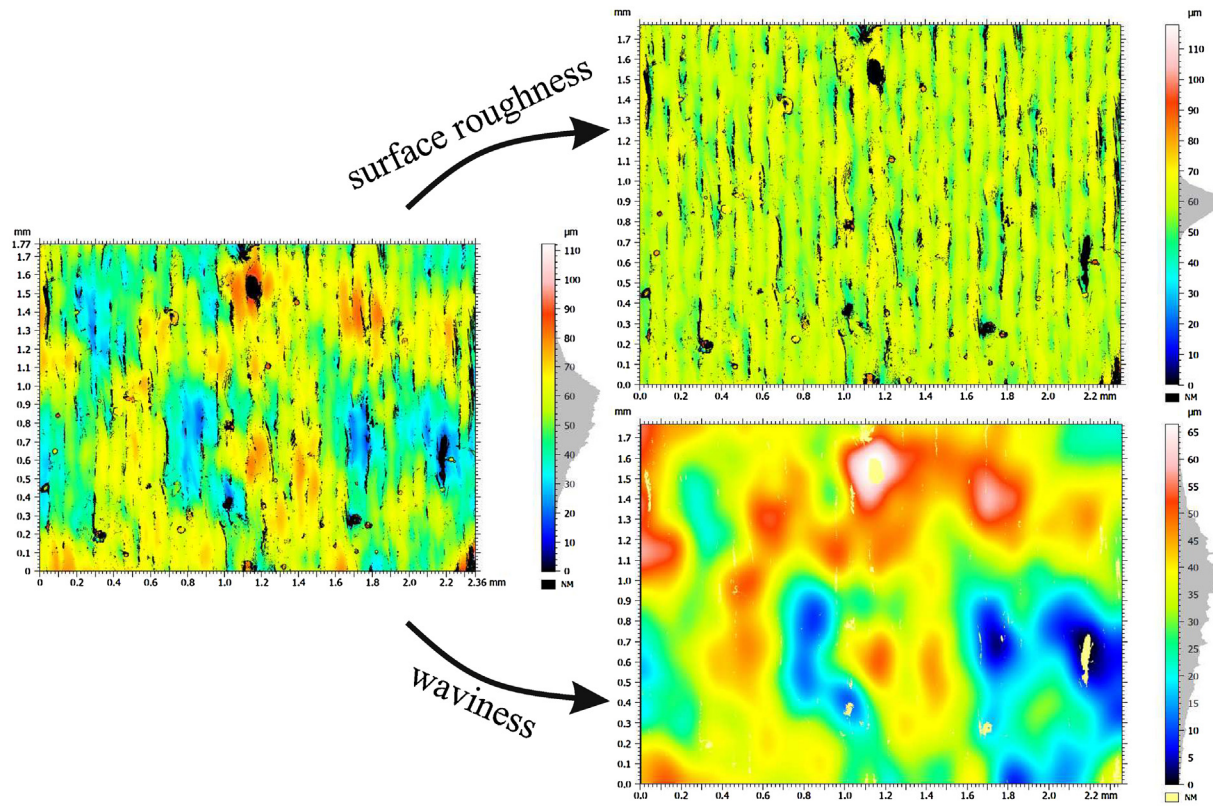


Fig. 7. Illustration of the difference between an unfiltered image and the filtered images with a cut-off length of 0.25 mm with one showing the roughness of wavelengths smaller than the cut-off length which is used for the further investigation and the other one showing the waviness with wavelength larger than the cut-off length.

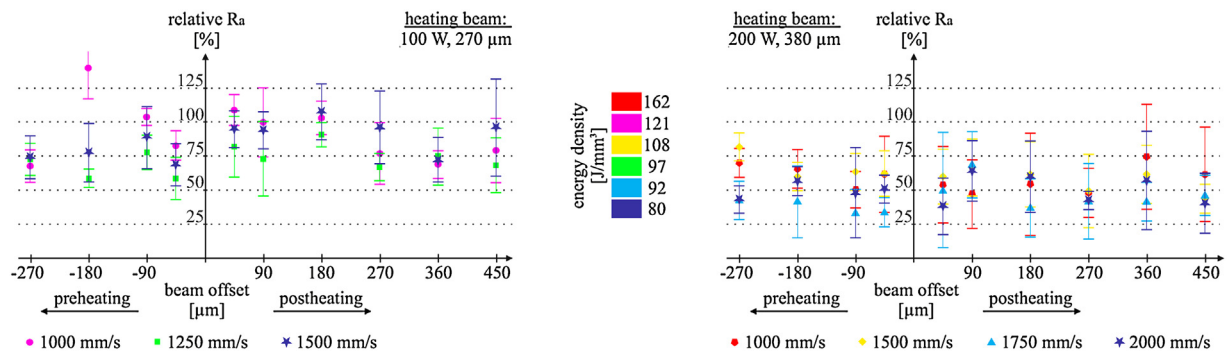


Fig. 8. Arithmetical mean deviation R_a and its standard deviations for the investigated parameter sets. The values are calculated by assessing ten profiles perpendicular to scanning direction for every parameter set and filtered with a cut-off length of 0.25 mm. The values are set in relation with the surface roughness of the same speed single-beam sample.

melting temperature after cooling down.

This explains the appearance of double melt pool boundaries which are commonly not observed in SLM. Furthermore, it clearly shows the influence of the second beam on the cool down phase of the melt pool. It can be expected that to a certain extent the distance between lower and upper melt pool boundary can be adjusted by carefully defining the beam offset. This influence on the cool down phase is especially effective when considering the very small melt pools of Fig. 6 which would commonly result in balling melt pools due to insufficient wetting and strong capillary forces when using a single beam. Yet, with the influence of a postheating beam the surface can be smoothed by changing the cool down phase.

5. Conclusion

The results show that multi-beam strategies that use a second beam with a larger beam diameter to heat the vicinity of the melt pool significantly influence the part's microstructure, surface roughness and density. The main results are the following.

1. In case of postheating offsets larger than 90 μm double melt pool boundaries can be observed because the solidification is briefly suspended by the second beam's energy input. Simulated temperature curves show that the solidification can even be reversed unto a certain depth for a small period of time by the heating beam.
2. The multi-beam strategies are resulting in smoother surfaces than the single-beam reference ones as long as the maximum heating power of 200 W is used.

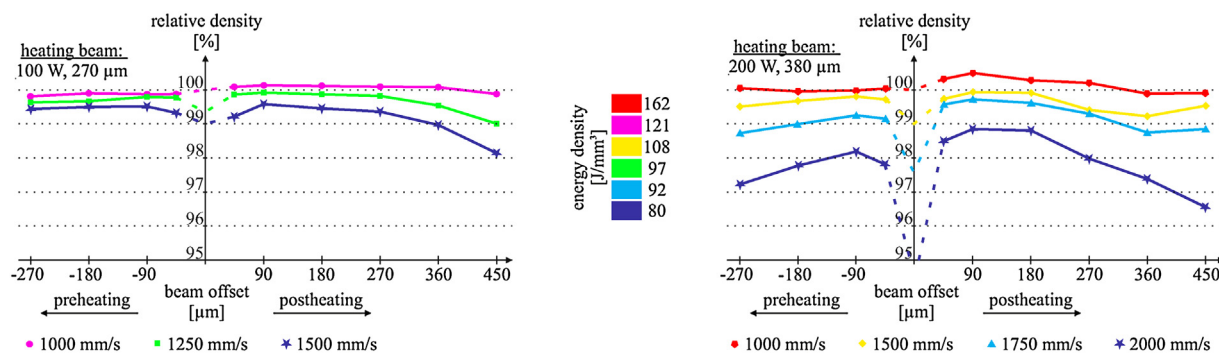


Fig. 9. Measured relative density values of the samples produced using the listed parameters. The values are set in relation to the density of a cube manufactured with 200 W at 1000 mm/s scan speed. The lines are colored in correlation to the energy density of the used parameter sets. Preheating sets are listed with a negative offset, postheating with positive offsets. The density values of same speed single beam samples processed at 200 W power are indicated by the dashed line intersection at 0 μm beam offset. (For interpretation of the references to color in this figure legend, the reader is referred to the web version of this article.)

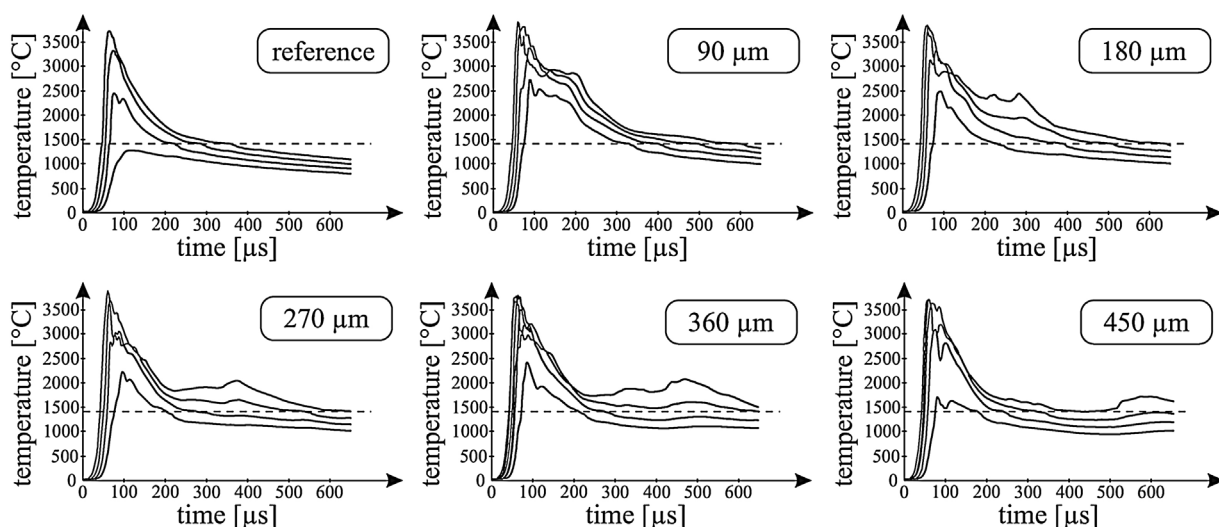


Fig. 10. Simulated temperature curves of a cross section at a heating power of 100 W and a heating beam diameter of 270 μm at different postheating offsets and a scan speed of 1000 mm/s. The lines represent elements at different depths within the melt pool cross section center. The elements are positioned 15 μm, 25 μm, 35 μm, 45 μm deep in the previous layer. The dashed line represents melting temperature.

3. Since the heating power is induced to the vicinity of the melt pool, the power can be used to increase the productivity as well, meaning at higher scan speeds similar density values can be achieved as at comparable energy densities, yet lower scan speeds, of a single beam, even though the input power is distributed over a far larger area. The amount of heating power that results in a density increase is dependent on the elaborated parameter set.
4. The highest densities are achieved for offsets of 90 μm for preheating as well as postheating. The density measurements indicate a negative interaction of the heat input of both beams for offsets as low as 45 μm.

These results underline the capability of multi-beam strategies within the selective laser melting process. These strategies offer a chance to reduce residual stresses, increase density and surface quality without losing a significant amount of productivity or flexibility.

Acknowledgments

The authors gratefully acknowledge the funding granted by the Bosch Research Foundation. And special thanks are given to Joao Eduardo Souza de Campos for his help with preparing the samples' cross sections.

References

- [1] P. Mercelis, J. Kruth, Residual stresses in selective laser sintering and selective laser melting, *Rapid Prototyp. J.* 12 (5) (2006) 254–265, <http://dx.doi.org/10.1108/1352540610707013>.
- [2] M.F. Zaeh, G. Branner, Investigations on residual stresses and deformations in selective laser melting, *Prod. Eng.* 4 (1) (2010) 35–45, <http://dx.doi.org/10.1007/s11740-009-192-y>.
- [3] J.-P. Kruth, J. Deckers, E. Yasa, R. Wauthle, Assessing and comparing influencing factors of residual stresses in selective laser melting using a novel analysis method, *Proc. Inst. Mech. Eng. Part B: J. Eng. Manuf.* 226 (6) (2012) 980–991, <http://dx.doi.org/10.1177/0954405412437085>.
- [4] J.P. Kruth, L. Froyen, J. Van Vaerenbergh, P. Mercelis, M. Rombouts, B. Lauwers, Selective laser melting of iron-based powder, *J. Mater. Process. Technol.* 149 (1–3) (2004) 616–622, <http://dx.doi.org/10.1016/j.jmatprotec.2003.11.051>.
- [5] M. Rombouts, J.P. Kruth, L. Froyen, P. Mercelis, Fundamentals of selective laser melting of alloyed steel powders, *CIRP Ann. - Manuf. Technol.* 55 (1) (2006) 187–192, [http://dx.doi.org/10.1016/S0007-8506\(07\)60395-3](http://dx.doi.org/10.1016/S0007-8506(07)60395-3).
- [6] M. Grasso, B.M. Colosimo, Process defects and in situ monitoring methods in metal powder bed fusion: a review, *Meas. Sci. Technol.* 28 (4) (2017) 044005, <http://dx.doi.org/10.1088/1361-6501/aa5c4f>.
- [7] T. Childs, C. Hauser, M. Badrossamay, Selective laser sintering (melting) of stainless and tool steel powders: experiments and modelling, *Proc. Inst. Mech. Eng. Part B: J. Eng. Manuf.* 219 (4) (2005) 339–357, <http://dx.doi.org/10.1243/095440505X8109>.
- [8] L. Rickenbacher, T. Etter, S. Hövel, K. Wegener, High temperature material properties of IN738LC processed by selective laser melting (SLM) technology, *Rapid Prototyp. J.* 19 (4) (2013) 282–290, <http://dx.doi.org/10.1108/13525413132381>.
- [9] A.B. Spierings, K. Dawson, T. Heeling, P.J. Uggowitzer, R. Schaeublin, F. Palm, K. Wegener, Microstructural features of Sc- and Zr-modified Al-Mg alloys processed

- by selective laser melting, Mater. Des. 115 (2017) 52–63, <http://dx.doi.org/10.1016/j.matdes.2016.11.040>.
- [10] B. Vrancken, L. Thijis, J.-P. Kruth, J. Van Humbeeck, Heat treatment of Ti6Al4V produced by selective laser melting: microstructure and mechanical properties, J. Alloys Compd. 541 (2012) 177–185, <http://dx.doi.org/10.1016/j.jallcom.2012.07.022>.
- [11] M. Cloots, K. Kunze, P.J. Uggowitzer, K. Wegener, Microstructural characteristics of the nickel-based alloy IN738LC and the cobalt-based alloy Mar-M509 produced by selective laser melting, Mater. Sci. Eng. A 658 (2016) 68–76, <http://dx.doi.org/10.1016/j.msea.2016.01.058>.
- [12] D.D. Gu, W. Meiners, K. Wissenbach, R. Poprawe, Laser additive manufacturing of metallic components: materials, processes and mechanisms, Int. Mater. Rev. 57 (3) (2012) 133–164, <http://dx.doi.org/10.1179/1743280411Y.0000000014>.
- [13] J.T. Sehrt, G. Witt, Dynamic strength and fracture toughness analysis of beam melted parts, Proc. 36th Int. MATADOR Conf. (2010) 385–388.
- [14] E. Brandl, U. Heckenberger, V. Holzinger, D. Buchbinder, Additive manufactured AlSi10Mg samples using selective laser melting (SLM): microstructure, high cycle fatigue, and fracture behavior, Mater. Des. 34 (2012) 159–169, <http://dx.doi.org/10.1016/j.matdes.2011.07.067>.
- [15] P.F. Kelley, J.K. Vlahakis, A. Carter, Tensile and fatigue behavior of direct metal laser sintered Inconel 718, Int. J. Precis. Technol. 6 (2016) 277–288.
- [16] H. Gong, K. Rafi, H. Gu, G.D. Janaki Ram, T. Starr, B. Stucker, Influence of defects on mechanical properties of Ti-6Al-4V components produced by selective laser melting and electron beam melting, Mater. Des. 86 (2015) 545–554, <http://dx.doi.org/10.1016/j.matdes.2015.07.147>.
- [17] W.E. King, A.T. Anderson, R.M. Ferencz, N.E. Hodge, C. Kamath, S.A. Khairallah, A.M. Rubenchik, Laser powder bed fusion additive manufacturing of metals; physics, computational, and materials challenges, Appl. Phys. Rev. 2 (4) (2015) 041304, <http://dx.doi.org/10.1063/1.4937809>.
- [18] M.J. Matthews, G. Guss, S.A. Khairallah, A.M. Rubenchik, P.J. Depond, W.E. King, Denudation of metal powder layers in laser powder bed fusion processes, Acta Mater. 114 (2016) 33–42, <http://dx.doi.org/10.1016/j.actamat.2016.05.017>.
- [19] M. Francois, A. Sun, W. King, N. Henson, D. Tourret, C. Bronkhorst, N. Carlson, C. Newman, T. Haut, J. Bakosi, J. Gibbs, V. Livescu, S. Vander Wiel, A. Clarke, M. Schraad, T. Blacker, H. Lim, T. Rodgers, S. Owen, F. Abdeljawad, J. Madison, A. Anderson, J.-L. Fattebert, R. Ferencz, N. Hodge, S. Khairallah, O. Walton, Modeling of additive manufacturing processes for metals: challenges and opportunities, Curr. Opin. Solid State Mater. Sci. 21 (4) (2017) 198–206, <http://dx.doi.org/10.1016/j.cossms.2016.12.001>.
- [20] S.A. Khairallah, A.T. Anderson, A. Rubenchik, W.E. King, Laser powder-bed fusion additive manufacturing: physics of complex melt flow and formation mechanisms of pores, spatter, and denudation zones, Acta Mater. 108 (2016) 36–45, <http://dx.doi.org/10.1016/j.actamat.2016.02.014> arXiv:arXiv:1011.1669v3.
- [21] P. Aggarangsi, J. Beuth, Localized preheating approaches for reducing residual stress in additive manufacturing, Proc. SFF Symp. Austin, 2006, pp. 709–720.
- [22] J. Wilkes, Y.-C. Hagedorn, W. Meiners, K. Wissenbach, Additive manufacturing of ZrO₂ Al₂O₃ ceramic components by selective laser melting, Rapid Prototyp. J. 19 (1) (2013) 51–57, <http://dx.doi.org/10.1108/13552541311292736>.
- [23] F. Abe, K. Osakada, M. Shiomi, K. Uematsu, M. Matsumoto, The manufacturing of hard tools from metallic powders by selective laser melting, J. Mater. Process. Technol. 111 (1–3) (2001) 210–213, [http://dx.doi.org/10.1016/S0924-0136\(01\)00522-2](http://dx.doi.org/10.1016/S0924-0136(01)00522-2).
- [24] T. Heeling, L. Zimmermann, K. Wegener, Multi-beam strategies for the optimization of the selective laser melting process, Proc. 27th Annu. Int. Solid Free. Fabr. Symp. doi:10.3929/ethz-a-010803938.
- [25] T. Heeling, K. Wegener, Computational investigation of synchronized multibeam strategies for the selective laser melting process, Phys. Procedia 83 (2016) 899–908, <http://dx.doi.org/10.1016/j.phpro.2016.08.094>.
- [26] T. Heeling, M. Gerstgrasser, K. Wegener, Investigation of selective laser melting spatter characteristics for single- and multi-beam strategies using high speed imaging, Proc. of LiM2017 Conf.
- [27] T. Heeling, M. Cloots, K. Wegener, Melt pool simulation for the evaluation of process parameters in selective laser melting, Addit. Manuf. 14 (2017) 116–125, <http://dx.doi.org/10.1016/j.addma.2017.02.003>.